

Effect of porosity on effective diagonal stiffness coefficients (c_{ii}) and elastic anisotropy of cortical bone at 1 MHz: A finite-difference time domain study

Cécile Baron,^{a)} Maryline Talmant, and Pascal Laugier

Université Pierre et Marie Curie-Paris 6, Laboratoire d'Imagerie Paramétrique, Paris F-75005, France
and CNRS, LIP, Paris F- 75006, France

(Received 16 March 2007; revised 12 June 2007; accepted 21 June 2007)

Finite-difference time domain (FDTD) numerical simulations coupled to real experimental data were used to investigate the propagation of 1 MHz pure bulk wave propagation through models of cortical bone microstructures. Bone microstructures were reconstructed from three-dimensional high resolution synchrotron radiation microcomputed tomography (SR- μ CT) data sets. Because the bone matrix elastic properties were incompletely documented, several assumptions were made. Four built-in bone matrix models characterized by four different anisotropy ratios but the same Poisson's ratios were tested. Combining them with the reconstructed microstructures in the FDTD computations, effective stiffness coefficients were derived from simulated bulk-wave velocity measurements. For all the models, all the effective compression and shear bulk wave velocities were found to decrease when porosity increases. However, the trend was weaker in the axial direction compared to the transverse directions, contributing to the increase of the effective anisotropy. On the other hand, it was shown that the initial Poisson's ratio value may substantially affect the variations of the effective stiffness coefficients. The present study can be used to elaborate sophisticated macroscopic computational bone models incorporating realistic CT-based macroscopic bone structures and effective elastic properties derived from μ CT-based FDTD simulations including the cortical porosity effect. © 2007 Acoustical Society of America. [DOI: 10.1121/1.2759165]

PACS number(s): 43.80.Ev, 43.80.Qf, 43.80.Jz, 43.80.Vj [FD]

Pages: 1810–1817

I. INTRODUCTION

Quantitative ultrasound has received considerable interest in recent years for its potential to assess different bone properties that are relevant to predict bone fragility.

Axial transmission is a generic term to designate a variety of techniques devised to assess cortical bone using a linear arrangement of ultrasound emitters and receivers placed on top of the overlying soft tissue. A part of the ultrasonic energy is guided along the cortex and can be radiated at the interface between soft tissue and bone. Various technical implementations of the technique have been proposed at different frequencies in the range 250 kHz–1.25 MHz.^{1–4}

Several wave types contribute to the total pressure field sensed by the receivers. The first arriving signal (FAS) is of special interest for *in vivo* assessment of cortical bone because it arrives prior to all other contributions, and therefore, can be easily determined from time-of-flight measurements of the signals received at different positions parallel to the interface.⁵ The nature of the wave associated with the first arriving signal was found to change with increasing cortical thickness to wavelength ratio ($\text{Cort.Th}/\lambda$) from an S_0 Lamb mode for $\text{Cort.Th}/\lambda \ll 1$ to a lateral wave for $\text{Cort.Th}/\lambda \gg 1$.⁶

Recently, axial transmission approaches have been described that work in a low frequency range and exploit a later

arriving signal, a slow guided wave mode, in addition to the FAS.^{4,7,8} This guided wave mode is well described by the theory for guided waves in plate [fundamental antisymmetric (or flexural) guided wave].²

Clinical trials revealed the ability of these techniques in discriminating normal and osteoporotic subjects.^{1,8,9} Clinical performances were enlightened by *in vitro* experiments. Experimental studies on excised human radii demonstrate the sensitivity of FAS velocity to porosity and degree of mineralization⁵ and also to intrinsic elastic properties.¹⁰ In addition, the velocity of the fundamental antisymmetric guided wave shows an exquisite sensitivity to cortical thickness.^{11,12}

Another approach used to give insight into clinical performances is the modeling of ultrasound propagation in axial transmission configuration. Bone finite-difference time domain (FDTD) studies, using either a generic model of the structure (plate or tube models)^{6,12} or bone structures reconstructed from three-dimensional x-ray tomography data, provided valuable insights into the relationships between ultrasound propagation characteristics (e.g., velocity of FAS or flexural mode) and bone properties such as cortical thickness and porosity. However, in these previous works, the models ignore the true local material properties, generic values were used instead.

We assume that the prediction capabilities of the computed tomography (CT) based finite-difference simulations may be enhanced with further refinements such as incorporating in the model individualized material properties.

^{a)}Electronic mail: norabelic@yahoo.fr

Bone is a poroelastic medium with a porous network filled with a fluid-like medium (marrow) embedded in an elastic tissue matrix. Cortical porosity mainly consists in an oriented network of Haversian canals of typically $50\ \mu\text{m}$ diameter approximately aligned with the long axis of the bone and of resorption cavities around $50\text{--}200\ \mu\text{m}$ in diameter. At a smaller scale, small transverse canaliculi and osteocytes lacunae (typically less than $10\ \mu\text{m}$ diameter) also contribute to cortical porosity. Each Haversian canal is surrounded by a layered cylindrical structure, called osteon, of typically $200\ \mu\text{m}$ diameter and between the osteons is the highly mineralized interstitial tissue. The wavelength in axial transmission is much longer than the typical size of these structures and the material properties required as input into the bone computational models are effective properties, the values of which are determined by the anisotropic elastic properties of the bone tissue matrix and by the oriented cortical porosity. First, the presence of pores inside the cortex induces a decrease of whole bone stiffness and density compared to stiffness and density of the bone matrix.¹³ Second, due to its preferential orientation, the porous network contributes to the mechanical anisotropy of bone.¹⁴ Progress in CT-based FDTD models requires knowing the effective individual material properties in which the effects of both cortical porosity and anisotropic elasticity are properly taken into account.

Scarce data on porosity-related anisotropic stiffness can be found in literature. Several experimental studies have investigated the impact of porosity on the longitudinal Young's modulus.^{15–18} As these studies were reduced to axial direction, they did not provide any information on the contribution of porosity to the anisotropy. A few studies, based on experiments or micromechanics models have examined the dependence of effective anisotropic stiffness coefficients on tissue properties and especially on porosity. Dependence on porosity of four elastic moduli of cortical bone assumed to be transversally isotropic has been reported in a single experimental study.¹³ Micromechanics provided comprehensive models of effective elastic properties of bone using various hypotheses to describe elastic properties of the bone matrix and the pore network.^{14,19} In particular, Sevostianov *et al.*¹⁴ have depicted the effect of porous network on overall stiffness coefficients of cortical bone assuming an isotropic bone matrix and identifying the effect of pore distribution. In the related field of composite media with unidirectional pores, a similar analysis was performed by Ichitsubo *et al.*²⁰ with an anisotropic matrix.

In this study, we report on microcomputed tomography (μCT) based FDTD simulations whereby the effective elastic properties are directly computed for individualized porous network of 19 cortical bone microstructures reconstructed from high resolution synchrotron radiation microtomography (SR- μCT). The bone matrix was modeled as a homogeneous anisotropic medium. As the elastic properties of the bone matrix were only partially documented in our samples, four built-in models were used for each specimen. The computational bone model for ultrasonic propagation in bone and the basis of the SR- μCT -based FDTD simulations are described in Sec. II. In Sec. III the results of the effective elastic prop-

erties are examined as a function of porosity for the different bone models. We close with a discussion of the limitations and potential extension of the current study.

II. MATERIALS AND METHODS

A. Samples

In this study we use a subset of 19 samples from a collection of human radii with soft tissue removed and previously assessed by different experimental techniques such as SR- μCT and scanning acoustic microscopy (SAM), which provided accurate data for cortical bone microstructure and estimates of material properties (density, stiffness) that were used to build the cortical bone models developed in the present paper.

Assessment of the microstructure was reported in Ref. 5. Small portions were cut in the postero-lateral zone of the distal radius. The dimensions were typically 10 mm long in the direction parallel to the bone axis and 8 mm long in the circumferential direction. These volumes were imaged by SR- μCT ²¹ at the European Synchrotron Radiation Facility (ESRF, Grenoble, France). The radiographs [two-dimensional (2D) projections] were recorded on a 1024×1024 charge-coupled device-based 2D detector and the voxel size was set to $10 \times 10 \times 10\ \mu\text{m}^3$. From sets of 2D projections under different angles of view, three-dimensional reconstructions of the microstructure were obtained by tomography algorithm. The amount of mineral was $1082 \pm 16\ \text{mg}/\text{cm}^3$ in the whole collection of samples.

Among the 19 samples considered in this study, 10 were previously studied by scanning acoustic microscopy at 50 MHz with a spatial resolution of $23\ \mu\text{m}$ and a spatial sampling rate of $20\ \mu\text{m} \times 20\ \mu\text{m}$.²² The section adjacent to the samples investigated by SR- μCT was scanned and a mapping of the acoustic impedance was provided. It was shown that the setup resolved Haversian canals larger than $25\ \mu\text{m}$. As a consequence, these measurements were representative of the impedance of the bone matrix at a scale of $20\ \mu\text{m}$. The acoustical impedance averaged over the whole set of specimens was found to be $8.1 \pm 0.5\ \text{MRa}$.

B. Configuration of the simulation

Propagation of transient 1 MHz plane waves in the 3D reconstructed bone microstructures was computed using a FDTD code, SIMSONIC, developed in the laboratory and detailed elsewhere,^{6,23} which computes a numerical solution to the 3D linear elastic wave propagation. The algorithm is based on Virieux scheme,²⁴ and uses first-order derivative in space and time.

The code requires the simulation box to be defined as right angle volume. Therefore, parallelepipedic volumes were extracted from the 3D SR- μCT reconstructed volumes (Fig. 1). The volume of the blocks analyzed in simulation with a spatial step of $20\ \mu\text{m}$ varies from 9 to $36\ \text{mm}^3$, depending on the thickness of the sample.

A combination of symmetric boundary conditions (tangential velocities equal on both sides of the boundary and normal velocities null on the boundary) and/or antisymmetric boundary conditions (tangential velocities null on the bound-



FIG. 1. Three-dimensional porous network (pores are in grey) in a parallel-epipedic block extracted from the μ CT reconstructed bone structure. On the right-hand side are shown a transverse and longitudinal cross section through the three-dimensional porous network. The preferential orientation of the pores is along the bone axis.

ary and normal velocities equal on both sides of the boundary) on the simulation domain was applied to ensure the propagation of compression and/or shear plane bulk waves. Perfectly matched layers (PML) on sides and edges of the simulation domain were used to avoid unphysical reflections.²⁵

SimSonic provides the transient signals associated with transmission of 1 MHz bulk compression or shear waves through the reconstructed volumes. Typical signals are shown in Fig. 2. Plane bulk waves velocities were deduced from time of flight measurements by detection of first signal maximum.

C. Derivation of effective stiffness

Effective stiffness coefficients were derived from velocities of simulated pure bulk wave propagating in principal directions and from effective mass density. For cortical bone the general degree of anisotropy is that of orthotropic material symmetry,²⁶ which is characterized by nine independent stiffness coefficients. The stiffness matrix can be expressed as follows using the abbreviated subscript notation:²⁷

$$C = \begin{pmatrix} c_{11} & c_{12} & c_{13} & 0 & 0 & 0 \\ c_{12} & c_{22} & c_{23} & 0 & 0 & 0 \\ c_{13} & c_{23} & c_{33} & 0 & 0 & 0 \\ 0 & 0 & 0 & c_{44} & 0 & 0 \\ 0 & 0 & 0 & 0 & c_{55} & 0 \\ 0 & 0 & 0 & 0 & 0 & c_{66} \end{pmatrix} \quad \begin{array}{l} X \leftrightarrow 1 \\ Y \leftrightarrow 2, \\ Z \leftrightarrow 3 \end{array} \quad (1)$$

where the X direction corresponds to the radial direction (i.e. thickness direction), the Y direction is the circumferential direction, and the Z direction is along the bone axis. But, as described by Katz,²⁸ the Haversian cortical bone is transverse isotropic in nature because of the locally uniaxial architecture of osteons. Consequently, numerous studies^{29–31} assumed the cortical bone as a transverse isotropic elastic solid medium, which reduces the number of independent coefficients of the stiffness matrix to five. Considering transverse isotropy with (XY) as the isotropic plane,^{32–34} the stiffness coefficients of C verify $c_{13}=c_{23}$, $c_{22}=c_{11}$, $c_{44}=c_{55}$, and $c_{66}=(c_{11}-c_{12})/2$.

When the waves propagate along principal directions of symmetry, the diagonal terms of the stiffness matrix c_{11} , c_{12} , and c_{33} are related to the phase velocity of compression-bulk wave which propagates along the X , Y , and Z direction, respectively, with

$$V_x = \sqrt{\frac{c_{11}}{\rho}}, \quad V_y = \sqrt{\frac{c_{22}}{\rho}}, \quad V_z = \sqrt{\frac{c_{33}}{\rho}}. \quad (2)$$

The stiffness coefficients c_{44} and c_{55} are related to the phase velocity of shear wave which propagate in Z direction and c_{66} in the transverse plane according to

$$V_{yz} = \sqrt{\frac{c_{44}}{\rho}}, \quad V_{xz} = \sqrt{\frac{c_{55}}{\rho}}, \quad V_{xy} = \sqrt{\frac{c_{66}}{\rho}}. \quad (3)$$

The effective stiffness coefficients were deduced from Eqs. (2) and (3) calculating the effective mass density ρ with the following rule of mixture:

$$\rho = \rho^0(1-p) + p\rho_w, \quad (4)$$

where ρ^0 is the mass density of the tissue matrix, ρ_w is the mass density of the fluid filling the pores (water), and p is the porosity.

D. Numerical bone models

Maps of the mass density and of the stiffness coefficients were used as input data in the software. The cortical bone was modeled as a two-phase medium constituted by the bone matrix and the fluid filling the pores. Each phase was supposed to be homogeneous within and between the samples. The spatial variation of density and stiffness in the simulation volume (spatial step of 20 μ m) relies on the presence of the pores. Both components were clearly delineated by segmentation of the original reconstructed SR- μ CT data and were defined by fixed mass density and stiffness coefficients.

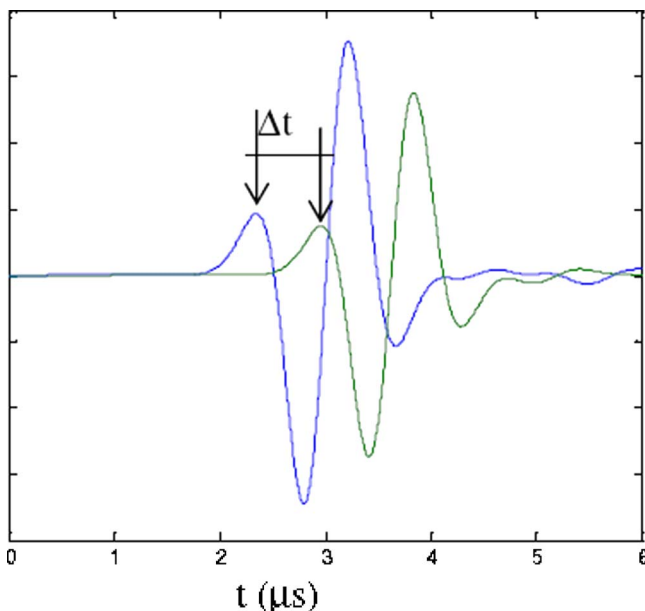


FIG. 2. (Color online) Velocity evaluation from the first maximum signal detection.

TABLE I. Four bone matrix models.

	c_{33}^0 (GPa)	c_{11}^0 (GPa)	c_{33}^0/c_{11}^0	c_{13}^0/c_{11}^0	c_{55}^0/c_{11}^0	c_{66}^0/c_{11}^0
Model 1	34.3	34.3	1	0.43	0.29	0.29
Model 2	34.3	30.6	1.12	0.42	0.34	0.29
Model 3	34.3	27.3	1.26	0.42	0.38	0.31
Model 4	34.3	22.9	1.5	0.41	0.45	0.30

Ideal nonviscous fluid (water) was assumed to fill the pores. The mass density was ($\rho_f=1 \text{ g/cm}^3$), and the stiffness coefficients were calculated from the following Lamé's constants values ($\lambda=2.25 \text{ GPa}$, $\mu=0 \text{ GPa}$).

Simulations in each bone sample microstructure were conducted with four different models of bone matrix shown in Table I. For the isotropic case (model 1), two independent stiffness coefficients are required (c_{33}^0 , c_{13}^0) to define the elasticity of the bone matrix, and in the three transversely isotropic models (models 2–4), five independent stiffness coefficients are needed (c_{11}^0 , c_{33}^0 , c_{55}^0 , c_{13}^0 , and c_{12}^0). Here, the subscript zero is used to denote the intrinsic stiffness of the tissue matrix.

In all the models, the axial stiffness c_{33}^0 was taken close to 34 GPa, the overall mass density ρ^0 of the bone matrix mass 1.91 g/cm^3 . These values were derived from SR- μ CT and SAM data averaged over the samples that were investigated with these techniques. In Ref. 22, the mass density of the solid matrix was related by a second-order polynomial fit to the mineral amount. According to this, the mass density in our study was approximated to a value of 1.91 mg/cm^3 , considering the mean value of mineralization previously measured and neglecting the intersample variations. The axial stiffness $c_{33}^0=34.3 \text{ GPa}$ was derived from acoustic impedance ($Z=8.1 \text{ MRa}$) values measured at 50 MHz, with a resolution of $23 \mu\text{m}$ well adapted to spatial grid of the simulation ($20 \mu\text{m}$). The axial stiffness was derived using the relation

$$c_{33}^0 = \frac{Z^2}{\rho^0} \quad (5)$$

between acoustical impedance and density, with $\rho^0 = 1.91 \text{ g/cm}^3$. Because the standard deviation of the acoustic impedance over the samples was small and the variations of the mean value of the acoustic impedance were weak between the different regions investigated, a fixed value of c_{33}^0 was adopted within and between specimens. We choose to couple the numerical simulations to experimental data obtained on the same set of specimens investigated by both scanning acoustic microscopy and μ CT. This might have resulted in stiffness values slightly higher than values reported in the literature.^{13,35} We do not expect the trends reported here to be accurate in an absolute sense. However, since our main conclusion is based on the comparative performance of the models, the general trends reported here are expected to hold in a relative sense. All four models are built around the same value of c_{33}^0 . It would be interesting to carry out a parametric study on the influence of this absolute value.

With models 2–4, transversely isotropic bone matrices with various degrees of anisotropy were explored. The value of the anisotropy ratio $AR_0=c_{33}^0/c_{11}^0$ was chosen in the range 1–1.5. The value of c_{11}^0 was therefore determined from the selected anisotropy ratio value. Moreover, for the three transversely isotropic matrix (models 2–4), the shear stiffness coefficient c_{55}^0 was fixed to 10.4 GPa.³⁶

The other stiffness coefficients, c_{13}^0 and c_{12}^0 , were derived from the relationship between Poisson's ratio and stiffness, assuming the bone matrix to be either isotropic (model 1) or transversely isotropic (models 2–4), with the following relationships:

$$\nu_L^0 = \frac{c_{13}^0}{c_{11}^0 + c_{12}^0}, \quad \nu_T^0 = \frac{c_{33}^0 c_{12}^0 - (c_{13}^0)^2}{c_{33}^0 c_{11}^0 - (c_{13}^0)^2}. \quad (6)$$

The longitudinal ν_L^0 and the transverse ν_T^0 Poisson's ratios were equal and set to a value of 0.3, a commonly used value in the literature.^{37–39} Model 2 was build with $AR_0=1.12$, a value reported in Hofmann *et al.*³⁶ In model 3, a ratio of anisotropy $c_{33}^0/c_{11}^0=1.26$ was adopted, according to Turner's report.³⁷ In addition, we kept in this model the value of the longitudinal shear modulus given in Ref. 36 providing c_{55}^0 .

Model 4 was used to enlarge the range of anisotropy ratio and AR_0 reaches the value of 1.5, the value of c_{33}^0 and c_{55}^0 remaining the same as in models 2 and 3.

E. Pore size and porosity

Figure 2 shows a typical 3D reconstruction of the porous network. To perform numerical simulation, the original grey scale reconstructions were segmented to yield binary mappings of the porous network. The segmentation threshold laid between the two well-separated distributions of pixel values

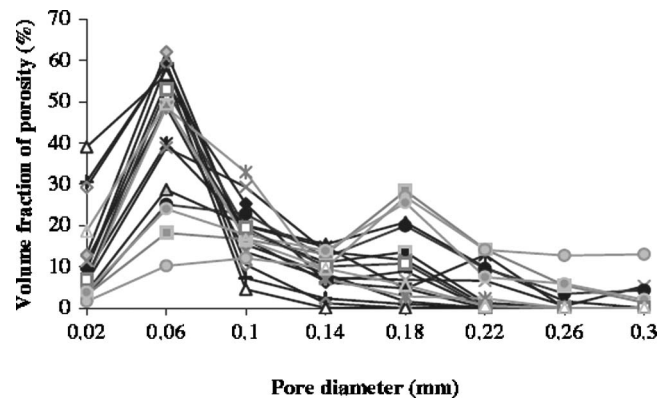


FIG. 3. Distribution of pores diameter through the 19 samples.

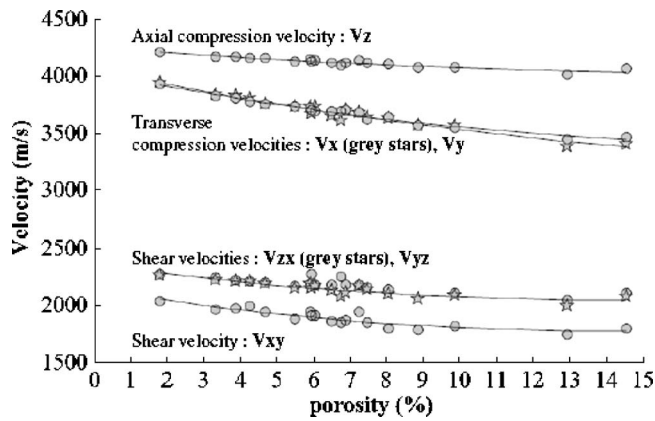


FIG. 4. Effective compression and shear bulk wave velocities deduced from FDTD simulations as a function of cortical porosity (model 2). The grey stars represent V_x and V_{zx} .

corresponding to the bone tissue and to the empty pores. The porosity was defined for each specimen as the ratio of the volume of pores to the total bone volume. The pore area related to different pore diameters was estimated in each reconstructed tomographic cross section, and then the pore areas were summed over the cross sections and multiplied by the spatial step increment between two consecutive slices to obtain the porosity. The distribution of the porosity as function of pore diameters was deduced from the morphological analysis of the 19 reconstructed microstructures. In addition, structural parameters such as mean pore density (number of detected pores per mm^2) and mean pore diameter (the equivalent diameter was determined from the area of the individual canals) were extracted.

III. RESULTS

A. Pore size and porosity

Each of the 19 samples had a porosity falling in the range 2%–15%. The distribution of diameters for the 19 specimens illustrated in Fig. 3 shows a bimodal distribution with two pore classes, the 60- and the 180- μm -diam groups, as contributors to the porosity (Fig. 3). The spatial resolution of SR- μCT was not sufficient to resolve the smallest pores (osteocytes lacunae, canaliculi) of a few microns in diameter. A higher resolution ($<10 \mu\text{m}$) is needed to consistently visualize all cortical pores in human bone.⁴⁰

The average porosity in these samples was about 7%, the average pore number density was 15 mm^{-2} , and the mean

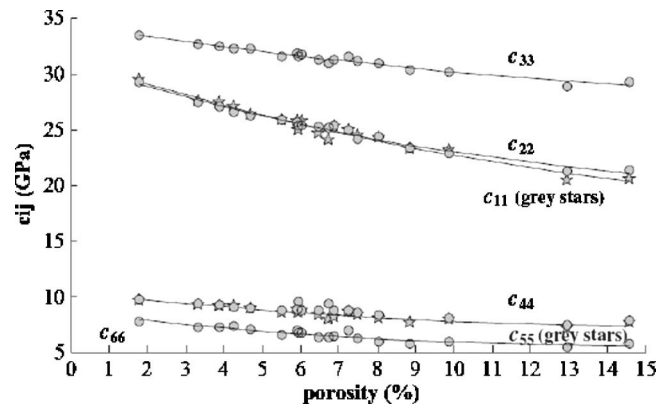


FIG. 5. Effective diagonal stiffness coefficients as a function of porosity (model 2).

pore diameter was about 80 μm . These results are consistent with previous morphological studies on human cortical bone.^{22,41}

B. Effective velocities and stiffness coefficients as a function of cortical porosity

Velocities of compression and shear bulk plane waves along the three principal axes of symmetry were computed for the 19 bone specimens and the 4 models. Figure 4 presents results for model 2. All the effective compression and shear bulk wave velocities decrease when porosity increases. However, the decrease was less pronounced for propagation along the long axis of the bone compared to the transverse directions. For a 10% increase in porosity, waves that propagate in the transverse plane undergo a decrease of 12% (470 m/s) for compression waves and 17% (370 m/s) for shear waves, while waves that propagate in the Z direction are reduced by 4% (160 m/s) for compression waves and 11% (260 m/s) for shear waves.

Similar trends of velocity variation versus porosity were observed for the four bone matrix models (Table II).

As a consequence of the decrease of both the effective mass density [Eq. (4)] and bulk wave velocities (Fig. 4) with the porosity, all the effective diagonal stiffness coefficients decline with the porosity as illustrated for model 2 in Fig. 5.

In all the bone models, a quadratic law between stiffness coefficients and porosity (ap^2+bp+c) was a better fit than a linear regression, although the first coefficient of the polynomial was small (see Table III).

TABLE II. Absolute (relative variation) of compression and shear waves velocities for a 10% increase of porosity (from 0 to 10%).

(m/s)	Compression waves in the transverse plane V_x and V_y	Compression wave in the axial direction V_z	Shear wave in the transverse plane V_{xy}	Shear waves in the axial direction V_{zx} and V_{yz}
Model 1	530 (12%)	190 (4.5%)	380 (17%)	250 (11%)
Model 2	470 (12%)	160 (4%)	370 (17%)	260 (11%)
Model 3	420 (11%)	150 (3.5%)	355 (17%)	200 (9%)
Model 4	350 (10%)	130 (3%)	320 (11%)	270 (11%)

TABLE III. Quadratic law variations of the diagonal stiffness coefficients vs porosity $c_{ii}=a(p\%)^2+bp\%+c$.

$AR^0=1.12$	c_{11}	c_{22}	c_{33}	c_{44}	c_{55}	c_{66}
a	0.024	0.026	0.011	0.004	0.013	0.014
b	-1.088	-1.047	-0.527	-0.232	-0.398	-0.412
c	31.15	30.82	34.37	10.14	10.47	80.60
R^2	0.97	0.98	0.96	0.80	0.88	0.88

C. Porosity contribution to effective anisotropy

The influence of porosity on effective stiffness is weaker in the axial direction (i.e., for c_{33} and for c_{44} and c_{55}) compared to the transverse directions (i.e., for c_{11} and c_{22} and for c_{66}), a result that contributes to the increase of the effective anisotropy as a function of porosity compared to the original elastic anisotropy of the bone matrix.

The effective anisotropy ratio ($AR=c_{33}/c_{11}$) normalized by the intrinsic anisotropy ratio of the bone matrix ($AR^0=c_{33}^0/c_{11}^0$) is plotted as a function of porosity for the four different bone models in Fig. 6. Normalized anisotropy ratios are consistently found to be greater than one and increasing with the porosity. The data indicate that the porosity contributes to the overall effective elastic anisotropy of bone structure. The higher the porosity, the higher its contribution to the bone elastic anisotropy. A 10% increase of porosity (from 0 to 10%) results in a relative increase of anisotropy ranging between 16% (for $AR^0=1.5$) and 20% (for the isotropic case) for the four bone matrix models studied.

Furthermore, the effective shear anisotropy ratio ($AR'=c_{55}/c_{66}$) increases with the porosity: For a 10% increase of porosity, the AR' is 16% greater for the isotropic case (model 1), 14% greater for models 2 and 3, and 12% greater for model 4.

The relative contribution of porosity to structural anisotropy of cortical bone is all the more important because the bone matrix is weakly anisotropic.

On the other hand, the other anisotropy ratios assessed by FDTD simulations (c_{ii}/c_{11}) were found to remain almost unchanged with the porosity.

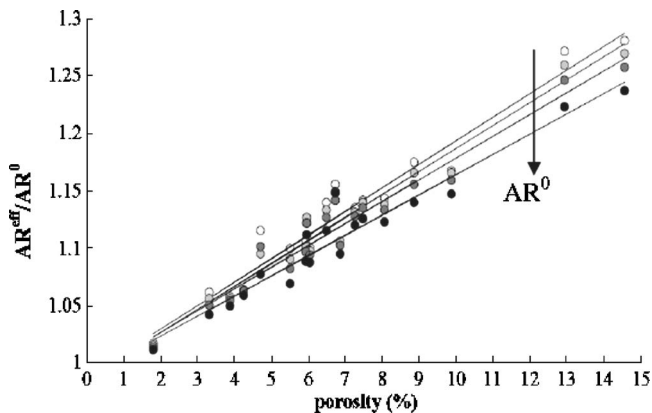


FIG. 6. Normalized effective anisotropy ratio (AR/AR_0) as a function of porosity for the different bone matrix models. Open circles correspond to the isotropic case (model 1), the light grey circles to model 2 ($AR^0=1.12$), the dark grey circles to model 3 ($AR^0=1.26$), and the closed circles to model 4 ($AR^0=1.5$).

IV. DISCUSSION

Our results suggest that the porous network introduces or reinforces transverse isotropy, as expected owing to its preferential orientation parallel to the bone axis. Indeed, it is noteworthy that the effect of porosity is similar for c_{11} and c_{22} , and for c_{44} and c_{55} . As pictured by Fig. 5, the differences between c_{11} and c_{22} and between c_{44} and c_{55} induced by the porous network were subtle: for example, $(c_{11}-c_{22})/c_{11} \leq 2 \times 10^{-4}$ for $p \leq 10\%$ and $(c_{11}-c_{22})/c_{11} \approx 4 \times 10^{-2}$ for $p \geq 10\%$. Therefore, if either isotropic (model 1) or transversely isotropic symmetry (models 2–4) is assumed for the tissue matrix, the introduction in the bone model of the oriented porous network resulted in a structure with effective transversely isotropic elastic properties. The result is consistent with the well-known effective macroscopic transverse isotropy of human cortical bone.^{34,42–44}

However, two additional conditions, $c_{13}=c_{23}$ and $c_{66}=(c_{11}-c_{12})/2$, required by this symmetry could not be checked here because mixed-indices stiffness coefficients were not evaluated. The evaluation of the mixed-indices stiffness coefficients c_{12} , c_{13} , and c_{23} requires one either to rotate the sample or to record angular variation of transmitted bulk wave. In the first case, it would be necessary to modify the software to implement capabilities of working with material of more general anisotropy than orthotropy, and in the second case it would be necessary to implement a more sophisticated signal processing. As these tasks were not under the scope of this study, the stiffness coefficients c_{12} , c_{13} , and c_{23} were not evaluated. However, note that under the reasonable assumption of a macroscopic transverse anisotropy, c_{12} can be simply derived from the knowledge of c_{11} and c_{66} with $c_{66}=(c_{11}-c_{12})/2$.

Coupling μ CT-based models of bone microstructure with FDTD simulations is a powerful means to compute the effect of porosity on effective stiffness and elastic anisotropy of bone. The high spatial resolution reached by SR- μ CT allows an accurate determination of the porous network. However, the bone computational model also requires input data for the stiffness of the bone tissue matrix. Because the complete set of real data (five stiffness coefficients and mass density) for the bone matrix was not known, some hypotheses were made. The Poisson's ratios are not easy to determine experimentally and therefore are not known with accuracy, and an *a priori* value of 0.3 for the Poisson's ratios was assumed, following a commonly adopted assumption in many studies, especially finite element analyses,⁴⁵ despite the rather wide range of values, between 0.12 and 0.63, reported in literature.^{31,42} Thus, one limitation of our study is related to the assumption adopted regarding the values of the

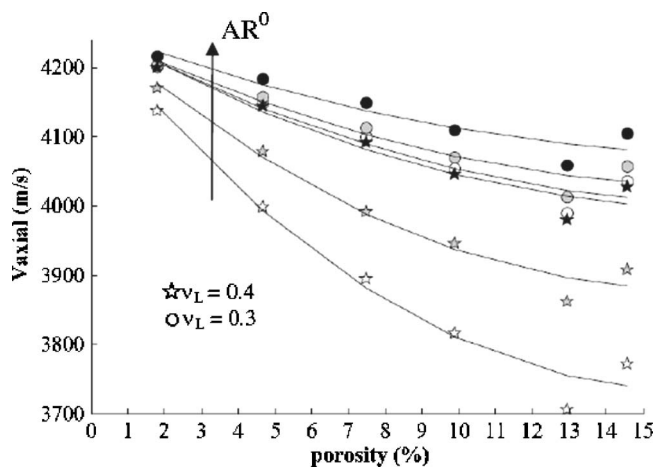


FIG. 7. Influence of the longitudinal Poisson's ratio on the dependence of the axial velocity on the cortical porosity. The stars represent the data obtained for $\nu_L=0.4$ and the circles represent the data related to $\nu_L=0.3$. The colors from white to black correspond to increasing AR^0 (model 1, model 2, and model 4).

Poisson's ratios, as mentioned in Raum *et al.*²² Here, in a first step we have investigated the influence of the longitudinal Poisson's ratio value on the axial velocity as a function of porosity for model 1 (model 1 is isotropic, the longitudinal and transverse Poisson's ratios are equal), model 2, and model 4. For these bone models, the computations have been run with an input Poisson's ratio value of 0.4 instead of 0.3. The new Poisson's ratio value was properly taken into account by modifying the value of the stiffness coefficients c_{12}^0 and c_{13}^0 according to Eq. (6).

The influence of the Poisson's ratio value on the axial velocity is presented in Fig. 7. The increase of Poisson's ratio from 0.3 to 0.4 induces a stronger impact of porosity on axial velocity and a better differentiation of the behavior between the different anisotropy models. For a longitudinal Poisson's ratio of 0.3 and a 10% increase of porosity, the axial velocity decreases by 190 m/s (4%) for model 1, 165 m/s (4%) for model 2, and 130 m/s (3%) for model 4. When the longitudinal Poisson's ratio is fixed to 0.4, the impact of a 10% increase of porosity on the axial velocity is of 430 m/s (10%) for model 1, 300 m/s (7%) for model 2, and 200 m/s (5%) for model 4. Consequently, an accurate estimation of the Poisson's ratios or of the related stiffness coefficients, especially the mixed-indices ones, at the matrix level is critical for a reliable prediction of relative variation of ultrasound velocities as function of porosity. Advances in this field have been published recently.^{31,45}

The present study permits a direct assessment of the effect of porosity on the stiffness coefficients of cortical bone. However, the morphology of the porous network is complex and requires several parameters to be fully characterized, including the size of the pores, pore density (number of pores per unit of area), spatial distribution of the pores, and shape of the pores.⁴⁶ The question arises as to whether these properties are determinant factors of the effective stiffness and the elastic anisotropy of cortical bone. Simplified models of porous networks were numerically built in order to better understand these effects for fixed values of porosity.

Preliminary results (not shown here) suggest that the influence of morphological parameters is small. For example, with a simplified model with a periodic spatial distribution of cylindrical inclusions embedded in the bone matrix, with their axis parallel to the axis of the bone, only subtle difference of 2% in the axial compression velocity could be observed. However, more work is required to explore the consequences of morphological variations in the cortical porosity on effective elastic properties.

The results of the present study can be used to elaborate sophisticated macroscopic computational bone models incorporating realistic CT-based macroscopic bone structures and effective elastic properties derived from μ CT-based FDTD simulations taking into account the effect of cortical porosity. These macroscopic computational bone models are of considerable interest as they can be used in order to evaluate the effect of porosity and of macroscopic bone structure on measured velocities in axial transmission. The frequency bandwidth (around 1 MHz) in this study is in the range of that typically used in some of the clinical settings. However, as mentioned in Sec. I, other devices are working at lower frequencies (around 250 kHz). Work on velocity frequency dispersion in cortical bone is sparse. Studying the frequency dependence of stiffness coefficients is potentially important. Therefore, specific attention must be paid in future works to the determination of phase velocity and amplitude in different frequency ranges.

V. CONCLUSION

The effect of oriented cortical bone porosity on ultrasound plane bulk wave velocities and elastic stiffness coefficients was investigated using transient numerical simulation of ultrasound plane bulk waves in 3D reconstructed microstructure of cortical bone samples. The effective stiffness coefficients were found to decrease with increasing porosity. The preferential orientation of the pore network along the bone axis induced an additional anisotropy (16%–20%) of the effective medium compared to the initial anisotropy of the bone tissue matrix. With initial Poisson's ratios values of 0.3, the variation of the effective anisotropy ratio was found to be fairly the same whatever the original anisotropy of the bone matrix was. However, the Poisson's ratio of the elastic bone matrix was found to be a critical determinant of the evaluation of relative variation of effective velocities and in turn of effective stiffness coefficients as a function of porosity.

¹D. Hans, S. K. Srivastav, C. Singal, R. Barkmann, C. F. Njeh, E. Kantorovitch, C. C. Gluer, and H. K. Genant, "Does combining the results from multiple bone sites measured by a new quantitative ultrasound device improve discrimination of hip fracture?," *J. Bone Miner. Res.* **14**, 644–651 (1999).

²P. Moilanen, P. H. F. Nicholson, T. Kärkkäinen, Q. Wang, J. Timonen, and S. Cheng, "Assessment of the tibia using ultrasonic guided waves in pubertal girls," *Osteoporosis Int.* **14**, 1020–1027 (2003).

³E. Bossy, M. Talmant, M. Defontaine, F. Patat, and P. Laugier, "Bidirectional axial transmission can improve accuracy and precision of ultrasonic velocity measurement in cortical bone: A validation on test materials," *IEEE Trans. Ultrason. Ferroelectr. Freq. Control* **51**, 71–79 (2004).

⁴A. Tatarinov, N. Sarvazyan, and A. Sarvazyan, "Use of multiple acoustic wave modes for assessment of long bones: Model study," *Ultrasonics* **43**, 672–680 (2005).

- ⁵E. Bossy, M. Talmant, F. Peyrin, L. Akrou, P. Cloetens, and P. Laugier, "An in vitro study of the ultrasonic axial transmission technique at the radius: 1-MHz velocity measurements are sensitive to both mineralization and intracortical porosity," *J. Bone Miner. Res.* **19**, 1548–1556 (2004).
- ⁶E. Bossy, M. Talmant, and P. Laugier, "Three-dimensional simulations of ultrasonic axial transmission velocity measurement on cortical bone models," *J. Acoust. Soc. Am.* **115**, 2314–2324 (2004).
- ⁷F. Lefebvre, Y. Deblock, P. Campistrion, D. Ahite, and J. J. Fabre, "Development of a new ultrasonic technique for bone and biomaterials in vitro characterization," *Biomedical Materials Res. Part B, (Applied Biomaterials)* **63**, 441–446 (2002).
- ⁸P. H. F. Nicholson, P. Moilanen, T. Kärkkäinen, J. Timonen, and S. Cheng, "Guided ultrasonic waves in long bone: Modelling, experiment and in vivo application," *Physiol. Meas.* **23**, 755–768 (2002).
- ⁹R. Barkmann, E. Kantorovich, C. Singal, D. Hans, H. K. Genant, M. Heller, and C. C. Glüer, "A new method for quantitative ultrasound measurements at multiple skeletal sites: First results of precision and fracture discrimination," *Clinical Densitometry* **3**, 1–7 (2000).
- ¹⁰K. Raum, I. Leguerney, F. Chandelier, E. Bossy, M. Talmant, A. Saied, F. Peyrin, and P. Laugier, "Bone microstructure and elastic tissue properties are reflected in QUS axial transmission measurements," *Ultrasound Med. Biol.* **31**, 1225–1235 (2005).
- ¹¹M. Muller, P. Moilanen, E. Bossy, P. H. F. Nicholson, V. Kilappa, J. Timonen, M. Talmant, S. Cheng, and P. Laugier, "Comparison of three ultrasonic axial transmission methods for bone assessment," *Ultrasound Med. Biol.* **31**, 633–642 (2005).
- ¹²P. Moilanen, V. Kilappa, P. Nicholson, J. Timonen, and S. Cheng, "Thickness sensitivity of ultrasound velocity in long bone phantoms," *Ultrasound Med. Biol.* **30**, 1517–1521 (2004).
- ¹³X. N. Dong and X. E. Guo, "The dependence of transverse elasticity of human femoral cortical bone on porosity," *J. Biomech.* **37**, 1281–1287 (2004).
- ¹⁴I. Sevostianov and M. Kachanov, "Impact of the porous microstructure on the overall elastic properties of the osteonal cortical bone," *J. Biomech.* **33**, 881–888 (2000).
- ¹⁵D. R. Carter and W. C. Hayes, "The compressive behaviour of bone as a two phase porous material," *J. Bone Jt. Surg., Am. Vol.* **59**, 954–962 (1977).
- ¹⁶J. D. Currey, "The effect of porosity and mineral content on the Young's modulus of elasticity of compact bone," *J. Biomech.* **21**, 131–139 (1988).
- ¹⁷T. S. Keller, Z. Mao, and D. M. Spengler, "Young's modulus, bending strength, and tissue physical properties of human compact bone," *J. Orthop. Res.* **8**, 592–603 (1990).
- ¹⁸S. Bensamoun, J.-M. Gherbezza, J.-F. de Belleval, and M.-C. Ho Ba Tho, "Transmission scanning acoustic imaging of human cortical bone and relation with the microstructure," *Clin. Biomech. (Los Angel. Calif.)* **19**, 639–647 (2004).
- ¹⁹X. N. Dong and X. E. Guo, "Prediction of cortical bone elastic constants by a two-level micromechanical model using generalized self-consistent method," *J. Biomech. Eng.* **128**, 309–316 (2006).
- ²⁰T. Ichitsubo, M. Tane, O. Hirotsugu, M. Hirao, T. Ikeda, and H. Nakajima, "Anisotropic elastic constants of lotus-type porous copper: Measurements and micromechanics modeling," *Acta Mater.* **50**, 4105–4115 (2002).
- ²¹M. Salome, F. Peyrin, P. Cloetens, C. Odet, A.-M. Laval-Jeantet, J. Baruchel, and P. Spanne, "A synchrotron radiation microtomography system for the analysis of trabecular bone samples," *Med. Phys.* **26**, 2194–2204 (1999).
- ²²K. Raum, R. O. Cleveland, F. Peyrin, and P. Laugier, "Derivation of elastic stiffness from site-matched mineral density and acoustic impedance maps," *Phys. Med. Biol.* **51**, 747–758 (2006).
- ²³E. Bossy, F. Padilla, F. Peyrin, and P. Laugier, "Three-dimensional simulation of ultrasound propagation through trabecular bone structures measured by Synchrotron tomography," *Phys. Med. Biol.* **50**, 5545–5556 (2005).
- ²⁴J. Virieux, "P-SV wave propagation in heterogeneous media: Velocity-stress finite-difference method," *Geophysics* **51**, 889–901 (1986).
- ²⁵F. Collino and C. Tsogka, "Application of the PML absorbing layer model to the linear elastodynamic problem in anisotropic heterogeneous media," *Geophysics* **66**, 294–307 (2001).
- ²⁶R. B. Ashman, S. C. Cowin, W. C. Van Burskirk, and J. C. Rice, "A continuous wave technique for the measurement of the elastic properties of cortical bone," *J. Biomech.* **17**, 349–361 (1984).
- ²⁷B. A. Auld, *Acoustic Fields and Waves in Solids*, Rob E. Krieger Publishing Company (Malabar, FL 1973).
- ²⁸J. L. Katz and K. Ukraincik, "On the anisotropic elastic properties of hydroxyapatite," *J. Biomech.* **4**, 221–227 (1971).
- ²⁹H. S. Yoon and J. L. Katz, "Ultrasonic wave propagation in human cortical bone. II. Measurement of elastic properties and microhardness," *J. Biomech.* **9**, 459–462 (1976).
- ³⁰J. L. Katz, "Anisotropy of Young's modulus of bone," *Nature (London)* **283**, 106–107 (1980).
- ³¹M. Pithioux, P. Lasaygues, and P. Chabrand, "An alternative ultrasonic method for measuring the elastic properties of cortical bone," *J. Biomech.* **35**, 961–968 (2002).
- ³²W. C. Van Burskirk, S. C. Cowin, and R. N. Ward, "Ultrasonic measurements of orthotropic elastic constants of bovine femoral bone," *J. Biomech. Eng.* **103**, 67–71 (1981).
- ³³J. L. Katz, H. S. Yoon, S. Lipson, R. Maharidge, A. Meunier, and P. Christel, "The effects of remodeling on the elastic properties of Bone," *Calcif. Tissue Int.* **36**, S31–S36 (1984).
- ³⁴J. Y. Rho, "An ultrasonic method for measuring the elastic properties of human tibial cortical and cancellous bone," *Ultrasonics* **34**, 717–783 (1996).
- ³⁵K. Hasegawa, C. H. Turner, and D. B. Burr, "Contribution of collagen and mineral to the elastic anisotropy of bone," *Calcif. Tissue Int.* **55**, 381–386 (1994).
- ³⁶T. Hofmann, F. Heyroth, H. Meinhard, W. Fränzel, and K. Raum, "Assessment of composition and anisotropic elastic properties of secondary osteon lamellae," *J. Biomech.* **39**, 2282–2294 (2006).
- ³⁷C. H. Turner, J. Y. Rho, Y. Takano, T. Y. Tsui, and G. M. Pharr, "The elastic properties of trabecular and cortical bone tissues are similar: Results from two microscopic measurement techniques," *J. Biomech.* **32**, 437–441 (1999).
- ³⁸J. Y. Rho, P. Zioupos, J. D. Currey, and G. M. Pharr, "Microstructural elasticity and regional heterogeneity in human femoral bone of various age examined by nano-indentation," *J. Biomech.* **35**, 189–198 (2002).
- ³⁹C. E. Hoffler, X. E. Guo, P. K. Zysset, and S. A. Goldstein, "An application of nano-indentation technique to measure bone tissue lamellae properties," *J. Biomech. Eng.* **127**, 1046–1053 (2005).
- ⁴⁰D. M. L. Cooper, J. R. Matyas, M. A. Katzenberg, and B. Hallgrímsson, "Comparison of microcomputed tomographic and microradiographic measurements of cortical bone porosity," *Calcif. Tissue Int.* **74**, 437–447 (2004).
- ⁴¹D. M. L. Cooper, A. L. Turinsky, C. W. Sensen, and B. Hallgrímsson, "Quantitative 3D analysis of the canal network in cortical bone by micro-computed tomography," *Anat. Rec.* **274B**, 169–179 (2003).
- ⁴²D. T. Reilly and A. H. Burstein, "The elastic and ultimate properties of compact bone tissue," *J. Biomech.* **8**, 393–405 (1975).
- ⁴³A. Ambaradar and C. D. Ferris, "Compact anisotropic bone: Elastic constants, in vitro aging effects and numerical results of a mathematical model," *Acta Biol. Acad. Sci. Hung.* **29**, 81–94 (1978).
- ⁴⁴S. Lipson and J. L. Katz, "The relationship between elastic and microstructure of bovine cortical bone," *J. Biomech.* **17**, 231–240 (1984).
- ⁴⁵R. Shahar, P. Zaslansky, A. A. Fiesem, J. D. Currey, and S. Weiner, "Anisotropic Poisson's ratio and compression modulus of cortical bone determined by speckle interferometry," *J. Biomech.* **40**, 252–264 (2007).
- ⁴⁶D. M. L. Cooper, A. L. Turinsky, C. W. Sensen, and B. Hallgrímsson, "Effect of voxel size on 3D micro-CT analysis of cortical bone porosity," *Calcified Tissue Int.* **80**, 211–219 (2007).